Quadrupolar particles in a nematic liquid crystal: Effects of particle size and shape

Francisco R. Hung*

Cain Department of Chemical Engineering, Louisiana State University, Baton Rouge, Louisiana 70803, USA

(Received 4 October 2008; revised manuscript received 16 December 2008; published 23 February 2009)

We investigate the effects of particle size and shape on the quadrupolar (Saturn-ring-like) defect structures formed by a nematic liquid crystal around nm-sized and μm-sized particles with spherical and spherocylindrical shapes. We also report results for the potentials of mean force in our systems, calculated using a mesoscale theory for the tensor order parameter **Q** of the nematic. Our results indicate that for pairs of nm-sized particles in close proximity, the nematic forms "entangled hyperbolic" defect structures regardless of the shape of the nanoparticles. In our calculations with nanoparticles we did not observe any other entangled or unentangled defect structures, in contrast to what was reported for pairs of μm-sized spherical particles. Such a finding suggests that the "entangled hyperbolic" defect structures are the most stable for pairs of nanoparticles in close proximity. For pairs of μm-sized particles, our results indicate that the nematic forms entangled "figure-of-eight" defect structures around pairs of spheres and spherocylinders. Our results suggest that the transition between "entangled hyperbolic" and figure-of-eight defect structures takes place when the diameter of the particle is between $D=100$ nm and 1 μm. We have also calculated the torques that develop when pairs of spherocylindrical nanoparticles in a nematic approach each other. Our calculations suggest that the nematic-mediated interactions between the nm-sized particles are fairly strong, up to 5700 k_BT for the case of pairs of spherocylindrical nanoparticles arranged with their long axis parallel to each other. Furthermore, these interactions can make the particles to bind together at specific locations, and thus could be used to assemble the particles into ordered structures with different morphologies.

DOI: 10.1103/PhysRevE.79.021705 PACS number(s): 61.30.Jf, 77.84.Nh, 61.30.Cz, 42.79.Kr

I. INTRODUCTION

Systems of particles dispersed in liquid crystals (LCs) have recently attracted attention for the development of novel materials based on the controlled assembly of the particles. The inclusion of the particles in the LC produces a distortion in its director field. As a result, both the colloids and the LC will reorganize as to minimize the elastic perturbations, giving rise to long-range interparticle interactions that can induce the formation of a number of ordered colloid structures [1–7]. The LC-mediated interparticle interactions are anisotropic and can be large, up to several thousands of k_BT, according to recent experimental measurements [1,3,4,6–11] and computer simulations [4,6–10,12–14]. Such interactions are reversible and disappear when the LC is driven into the isotropic phase. The LC-mediated colloidal interactions depend on the size and shape of the particles, the local anchoring of the LC at the surface of the colloids, the alignment of the director field far away from the particles, and the geometry of the surroundings (i.e., presence of walls, channels and other confining elements).

Most of the experimental work mentioned above has focused on systems of spherical, micron-sized colloids in LCs. A number of experimental studies (for reviews see, e.g., Ref. [15]) have considered systems of nanoparticles in LCs. LCs have been used to manipulate and organize spherical [16–20], as well as rodlike nanoparticles such as nickel nanowires and carbon nanotubes [21–24]. These systems have potential applications in light-scattering devices, electro-optical switches, electromechanical actuators, functional coatings, photonics, nanoscale electronics, and LC displays. The behavior of systems of nanoparticles in LCs is also relevant for the development of optical sensors. Recent experiments [25–28] and calculations [29–31] have demonstrated that the binding of chemicals, biomolecules, and viruses at solid-LC and liquid-LC functionalized interfaces perturbs the local ordering of the LC, and triggers the formation of inhomogeneous textures. Due to the long-range order of the LC, these inhomogeneities can be amplified over several length scales and detected using polarized optical microscopy.

The behavior of a dispersion of particles in LCs is dictated by the formation of defects around the particles. The uniform alignment of a LC is usually distorted by the inclusion of particles, due to the local constraints imposed by the anchoring of the LC at the surfaces of the particles. These constraints impose conflicting orientations to the liquid crystal, which results in the formation of topological defects. These defects are characterized by discontinuities in the director field $\mathbf{n}(\mathbf{r})$, strong biaxiality and a pronounced decrease in the scalar order parameter $S(\mathbf{r})$, reflecting the fact that the LC locally melts at the defect core [32]. For the simplest case of a single spherical particle in a nematic liquid crystal, three types of defects have been observed experimentally: the dipole configuration (where the nematic forms a point defect known as hyperbolic hedgehog) [1,33], the Saturn ring or quadrupolar configuration (where the particle is surrounded by a disclination loop) [33–35], and the surface ring configuration (where the nematic forms a disclination ring sitting at the surface of the particle) [1,33]. These defect structures have been the focus of several theoretical and computational studies [33,36–41]. The dipole configuration was found to be stable for strong surface anchoring and micron-sized spherical particles. The Saturn ring (quadrupolar) configuration

*frhung@lsu.edu

was predicted to become stable upon reduction of particle size, which was confirmed experimentally very recently [42]. Magnetic and electric fields [43], and confinement conditions [35,40,44] were also shown to stabilize a Saturn ring configuration. A surface ring defect is observed upon reduction of the surface anchoring strength [33,38]. Systems involving two spherical particles exhibiting dipole [45] and Saturn ring [12] configurations have been recently examined using a mesoscale theory where the nematic is described using the tensor order parameter $\mathbf{Q}(\mathbf{r})$. In the latter series of studies, the predictions of the mesoscale theory were compared to those of molecular simulations, thereby providing a measure of the validity of the theory at nm-length scales. Given the good agreement between the defect structures and the potentials of mean force obtained from Monte Carlo simulations and the mesoscale theory, the latter approach (which is computationally less expensive) was used to study the stability of arrays of several spherical nanoparticles in a nematic in the bulk [12] and inside channels of nanoscopic dimensions [14]. The continuum approach was also used to study the stability of arrays of spherocylindrical nanoparticles in a nematic [13]. Classical density functional theory has been used recently to study the structure of a LC around a cylindrical particle of infinite length and to calculate the forces between two of these particles [46]. Very recently, several groups have performed dynamical simulations in 2D and 3D systems, where disks or spherical particles are free to move due to the many-body forces mediated by the LC [47–50].

Recent calculations for systems of spherical nanoparticles in a nematic [12] indicate that when two spherical nanoparticles are close to each other, the nematic forms a defect structure consisting of one large Saturn ring (which arises from the fusion of the two Saturn rings that surround each particle when they are far from each other) and another disclination ring, which is orthogonal to the first one and forms in the interparticle space [see, e.g., Fig. 3(a)]. Hung *et al.* [13] also observed similar defect structures for systems of spherocylindrical nanoparticles in a nematic. These defect structures were also observed by other groups in recent experimental [9] and computational [9,48] studies involving systems of micron-sized spherical particles in a nematic liquid crystal. In these studies [9,48] it was argued that these quadrupolar defect structures, termed "entangled hyperbolic" by Ravnik *et al.* [9], were metastable and thus eventually evolve into another entangled defect structure with the shape of a "figure of eight" [9,48]. Such a defect structure consists of a single disclination loop that is twisted in the interparticle space and surrounds both particles [see, e.g., Fig. 3(b)]. Nevertheless, one fundamental difference between these studies is that Ravnik *et al.* [9] and Araki and Tanaka [49] considered micron-sized particles, whereas de Pablo *et al.* [12,13] studied nm-sized particles. Furthermore, these studies used different versions of a mesoscale theory in terms of $\mathbf{Q}(\mathbf{r})$, also with different numerical parameters. Moreover, de Pablo *et al.* [12,13] considered the case of infinitely strong homeotropic anchoring at the particles' surfaces, whereas Ravnik *et al.* [9] and Araki and Tanaka [49] also studied homeotropic anchoring but subject to a finite value of the anchoring constant W.

The objective of this paper is twofold. First, we use the same mesoscale theory and numerical parameters as proposed by Ravnik *et al.* [9], to consider a system with a pair of nm-sized spheres and another with two micron-sized spheres. With such a study we aim at establishing how the entangled defect structures change with the size of the particles. However, it is not our objective to determine the exact particle size at which the transition between entangled defect structures occurs; such an objective could be the subject of follow-up studies. The second objective of our study is to determine the nature of the defect structures formed around nm-sized and micron-sized spherocylindrical particles with different aspect ratios [21–24]. In all cases, the stability of the systems will be determined by calculating their free energies. The formation of defect structures around groups of particles in a nematic is important since strong, anisotropic interparticle interactions usually develop. Furthermore, the strength and degree of anisotropy in the interparticle interactions is expected to vary when particles of shape other than spherical are considered. These interparticle interactions can thus be used to direct the spherical and nonspherical particles to assemble into ordered arrays with a number of different morphologies, which is a subject that has attracted a great deal of attention recently [51,52]. The paper is organized as follows. In Sec. II we present a description of our model systems and details of the computational methodology. Section III contains our results and discussion, and our concluding remarks are presented in Sec. IV.

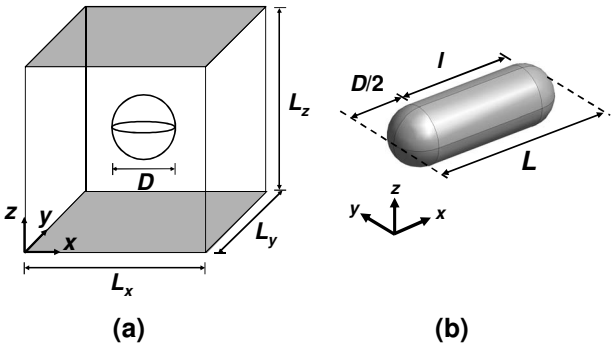

FIG. 1. Schematic representation of (a) model system and one spherical particle and (b) spherocylindrical particle.

II. MODELS AND METHODS

A. Details of the model systems

The model system considered in this work consists of a rectangular box of dimensions L_x, L_y, and L_z, containing one or two particles immersed in a nematic liquid crystal. A schematic representation of the model system for one spherical particle is shown in Fig. 1(a). Periodic boundary conditions are imposed in the x and y directions of the simulation box. We have placed walls at the top and bottom faces of the simulation box, imposing homeotropic anchoring to the liquid crystal (LC). Homeotropic anchoring is also imposed to the LC at the surfaces of the particles. Such conditions can be easily achieved experimentally, e.g., by coating the surfaces with self-assembled monolayers of alkanethiols [53]. In the absence of particles, the system exhibits a homogeneous texture in which the director field $\mathbf{n}(\mathbf{r})$ of the nematic is

TABLE I. Summary of the relevant dimensions of the systems considered in this study.

System	Particle size			Box size		
	D (μm)	L (μm)	f (μm)	L_x (μm)	L_y (μm)	L_z (μm)
Spheres, nm sized	0.100			1.17	0.520	0.200
Spheres, μm sized	1.00			3.00	2.00	2.00
Spherocylinders, nm sized, $L/D=1.44$, linear	0.100	0.144		1.17	0.520	0.200
Spherocylinders, μm sized, $L/D=1.44$, linear	1.00	1.44		4.00	2.00	2.00
Spherocylinders, nm sized, $L/D=1.44$, parallel	0.100	0.144		0.780	0.780	0.200
Spherocylinders, μm sized, $L/D=1.44$, parallel	1.00	1.44		2.40	3.00	2.00
Spherocylinders, nm sized, $L/D=3.00$, linear	0.100	0.300		1.17	0.520	0.200
Spherocylinders, μm sized, $L/D=3.00$, linear	1.00	3.00		7.00	2.00	2.00
Spherocylinders, nm sized, $L/D=3.00$, parallel	0.100	0.300		0.780	0.780	0.200
Spherocylinders, μm sized, $L/D=3.00$, parallel	1.00	3.00		4.00	3.00	2.00

parallel to the z axis. Strong variations in the director field and in the scalar order parameter $S(\mathbf{r})$, as well as topological defects are observed when particles are inserted, due to the conflicting orientations imposed to the nematic by the homeotropic anchoring conditions.

In this study we considered μm- and nm-sized particles of spherical and spherocylindrical shape. The spherical particles have a diameter D, whereas the spherocylindrical particles consist of a cylinder of length l terminated by spherical caps of diameter D, so that the total length of the spherocylinder is equal to $L=l+D$ [Fig. 1(b)]. The relevant dimensions of the systems considered in this study are summarized in Table I. We only considered systems of two particles in this work. In most cases, the centers of the particles were placed in the center of the simulation box, in the plane $z=0$. For the case of spherocylindrical particles, we considered two arrays where the particles have their long axis oriented along the x direction, but their centers are placed in different ways (Fig. 5): (a) centers are on the x axis (linear array) and (b) centers are on the y axis (parallel array).

B. Landau–de Gennes theory for the nematic liquid crystal

The behavior of the nematic was modeled using a mesoscale theory for the tensor order parameter $\mathbf{Q}(\mathbf{r})$, which is free of discontinuities even at the defect cores where the director field $\mathbf{n}(\mathbf{r})$ becomes discontinuous. The local values of the scalar order parameter $S(\mathbf{r})$ and the director $\mathbf{n}(\mathbf{r})$ can be obtained from $\mathbf{Q}$ through its largest eigenvalue $2S/3$ and its associated eigenvector [32]. In previous studies of spherical nanoparticles in a nematic [12], results for the potentials of mean force and the defect structures from the theory were compared with those from molecular simulations. In the latter methodology the nematic was represented as Gay-Berne ellipsoids. The researchers found good agreement between both simulation procedures, down to length scales comparable to the size of a LC molecule. Such a comparison provides a measure of the validity of the mesoscale theory even at nanometer length scales. The theory corresponds to a particular case of the Beris-Edwards formulation of the thermodynamics of fluids with internal microstructure [54]. The free energy F of the liquid crystal includes three contributions

$$F = \int dVf + \oint dSf_s = \int dVf_{\mathrm{LdG}} + \int dVf_e + \oint dSf_s. \tag{1}$$

For these three terms we have adopted the same expressions used by Škarabot *et al.* and Ravnik *et al.* in their studies [8–10]. The first term in Eq. (1), f_{LdG}, represents a Landau–de Gennes expansion [32] describing the short-range interactions that drive the bulk isotropic-nematic phase transition

$$f_{\mathrm{LdG}} = \frac{A}{2}Q_{ij}Q_{ji} + \frac{B}{3}Q_{ij}Q_{jk}Q_{ki} + \frac{C}{4}(Q_{ij}Q_{ji})^2, \tag{2}$$

where $i,j,k \in x,y,z$, and the Einstein summation convention over repeated indexes is used. The phenomenological coefficients A, B, and C depend on the specific nematic liquid crystal. The second term in Eq. (1) describes the long-range elastic forces of the liquid crystal, and introduces a free energy penalty associated with gradients of the tensor order parameter field. For simplicity, in our calculations we have used the one-elastic-constant approximation [32], where the splay, twist, and bend elastic constants K_{11}, K_{22}, and K_{33} have a common value. In our previous simulation study for systems of spherocylindrical nanoparticles in a nematic [13], we obtained similar results for the defect structures and potentials of mean force when we used the one-elastic-constant approximation and a three-constant expression that is cubic in $\mathbf{Q}$ and its gradients [54,55]. The elastic free energy in the one-elastic-constant approximation takes the form

$$f_e = \frac{L_1}{2}\frac{\partial Q_{ij}}{\partial x_k}\frac{\partial Q_{ij}}{\partial x_k}, \tag{3}$$

where the constant L_1 is related to the elastic constants K_{11}, K_{22}, and K_{33} by the following relations [54]: $2L_1=K_{11}/S^2=K_{22}/S^2=K_{33}/S^2$. The third term in Eq. (1) represents the surface contribution to the free energy, and accounts for the liquid crystal anchoring at the surfaces

$$f_s = \frac{W}{2}(Q_{ij} - Q_{ij}^0)(Q_{ji} - Q_{ji}^0), \tag{4}$$

where W is a constant representing the strength of the surface anchoring and Q_{ij}^0 is the preferred orientation of $\mathbf{Q}$ at the surfaces. We have only considered the case of strong homeotropic anchoring at all surfaces. All the values of the numerical parameters are the same as those used by Škarabot *et al.* and Ravnik *et al.* [8–10], which are representative of a low molecular-weight liquid crystal (e.g., 5CB): $A=-0.172\times10^6$ J/m^3, $B=-2.12\times10^6$ J/m^3, $C=1.73\times10^6$ J/m^3, $L_1=4.0\times10^{-11}$ N. These values give a bulk scalar order parameter of $S_{\text{bulk}}=0.533$ and a nematic coherence length (i.e., a characteristic length scale for spatial variations of $\mathbf{Q}$) [56] of $\xi_N=6.63$ nm [8–10]. We have used different values of W as to ensure that all our systems exhibit strong (but finite) homeotropic anchoring. In their studies, Škarabot *et al.* [8] fixed $W=10^{-2}$ J/m^2 for a spherical particle of radius $R=0.5$ μm, corresponding to a reduced extrapolation length [33,38] of $\xi_S=L_1/(WR)=0.008$. We kept the same value of $W=10^{-2}$ J/m^2 for our μm-sized particles ($D=1$ μm) and for our nm-sized particles ($D=100$ nm). For the latter case, we also obtained results using $W=0.1$ J/m^2; such a value was used in order to obtain the same extrapolation length ξ_S as in the study of Škarabot *et al.* [8]. We have performed simulations for nm-sized particles with values of W as high as 10.0 J/m^2, without finding any appreciable difference from the results obtained for the case of $W=0.1$ J/m^2.

The behavior of the tensor order parameter $\mathbf{Q}$ as a function of position $\mathbf{r}$ is determined by minimizing the free energy F [Eqs. (1)–(4)] according to the Euler-Lagrange formalism, which leads to the following partial differential equations for $\mathbf{Q}$ [8–10]:

$$-[AQ_{ij} + BQ_{ik}Q_{kj} + CQ_{ij}(Q_{kl}Q_{lk})] + L_1\frac{\partial}{\partial x_k}\left(\frac{\partial Q_{ij}}{\partial x_k}\right) = 0, \tag{5}$$

$$L_1\frac{\partial Q_{ij}}{\partial x_k}\nu_k + W(Q_{ij} - Q_{ij}^0) = 0. \tag{6}$$

Equation (5) governs the behavior of $\mathbf{Q}$ away from the surfaces, and represents a system of partial differential equations. All the surfaces in the system are subject to the boundary conditions given by Eq. (6), which determines the behavior of $\mathbf{Q}$ at the surfaces. Following our previous studies [13,14], in this work we have numerically solved the following equivalent time-dependent problem, ensuring that t is long enough as to observe negligible time variations in $\mathbf{Q}$:

$$-[AQ_{ij} + BQ_{ik}Q_{kj} + CQ_{ij}(Q_{kl}Q_{lk})] + L_1\frac{\partial}{\partial x_k}\left(\frac{\partial Q_{ij}}{\partial x_k}\right) = \frac{\partial Q_{ij}}{\partial t} \cong 0. \tag{7}$$

The system of equations given by Eq. (7), subject to the surface boundary conditions (6), was solved for the five independent components of $\mathbf{Q}$ (Q_{xx}, Q_{yy}, Q_{xy}, Q_{xz}, and Q_{yz}, since $\mathbf{Q}$ is traceless) using finite elements and the COMSOL Multiphysics package [57]. The initial conditions of $\mathbf{Q}$ in our simulations are such that the scalar order parameter S was initially fixed to the equilibrium value $S_{\text{bulk}}=0.533$; the scalar order parameter at the nanoparticles' surface was also set to $S=S_{\text{bulk}}$. The director $\mathbf{n}(\mathbf{r})$ was initially aligned along the z direction. In order to solve the equations, we used the time-dependent algorithm DASPK, combined with the linear system solver GMRES and the incomplete LU preconditioner [57]. Following our previous studies [13,14], we performed three-dimensional simulations using unstructured meshes containing tetrahedral, linear Lagrange elements automatically generated by COMSOL [58]. Different grid densities were used, and it was found that up to 66 000 finite elements were required for the numerical solutions to be independent of further mesh refinements. The mesh was significantly finer in the immediate vicinites, where important curvature effects and strong variations in $\mathbf{Q}$ are present. In all our simulations, the minimum length of the finite elements in our finest grid size is approximately $1.1\times10^{-4}D$, which is comparable to that reported by Fukuda *et al.* [39] in their adaptive mesh refinement scheme. Different methods are available to depict the NLC defect structures (the regions where the director field of the nematic becomes discontinuous) [59,60]. In this work, we have followed the work of Škarabot *et al.* and Ravnik *et al.* [8–10] and adopted the contour $S=0.48$ to visualize defects around μm-sized particles in 3D. For nm-sized particles, the isosurfaces of $S=0.48$ lead to defect cores that looked somewhat thick. Therefore we have followed our previous work [13,14] and used the contour $S=0.30$ instead, which is approximately the smallest value of S that leads to a stable bulk nematic for our theoretical model [54,56]. The free energy values used in the computation of the potential of mean force (PMF) were determined by numerical integration of Eqs. (1)–(4) over the volume and the surfaces of the system. For the case of spherocylindrical particles, we also computed the total torque $\mathbf{T}$ transmitted by the nematic to each spherocylinder using the following equation [61]:

$$\mathbf{T} = \oint \mathbf{L}\boldsymbol{\nu}dS, \tag{8}$$

Where $\boldsymbol{\nu}$ is the vector normal to the surfaces of the spherocylinders and the integration is done on the surfaces of each of the spherocylinders. $\mathbf{L}$ is the couple stress tensor [61]

$$L_{ij} = 2\varepsilon_{ikl}Q_{km}\frac{\partial f}{\partial(\partial Q_{ml}/\partial x_j)}, \tag{9}$$

where ε_{ikl} is the Ricci's alternator and f is the free energy volume density introduced in Eq. (1) as $\int dVf$. The components of the torque transmitted by the nematic to each spherocylinder were computed via numerical integration of Eqs. (8) and (9).

III. RESULTS AND DISCUSSION

A. Spherical particles

We first considered a system of two spherical particles in a nematic, aiming at elucidating how the size of the particles affect the morphology of the entangled defect structures

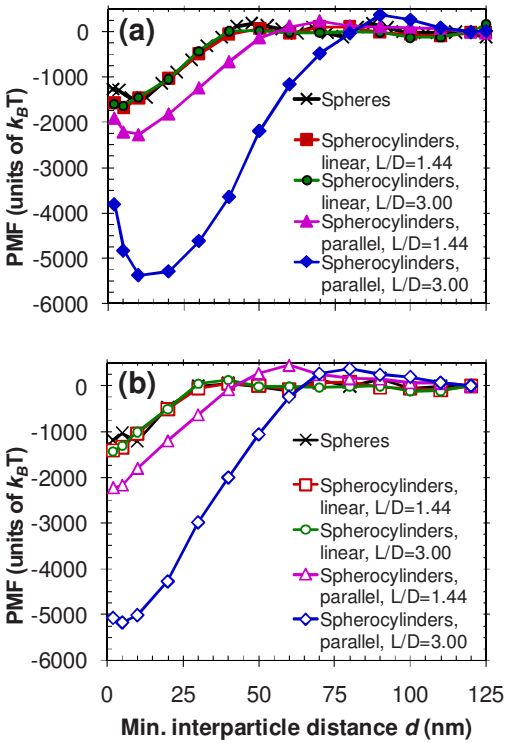

FIG. 2. (Color online) Potential of mean force (PMF) as a function of the minimum surface-to-surface interparticle distance d, for all the two-nanoparticle systems considered in this study. Two different values for the surface anchoring strength were considered: (a) $W=0.1$ J/m^2 and (b) $W=0.01$ J/m^2.

formed when the particles are close to each other. First we studied systems with two spherical nanoparticles ($D=100$ nm) approaching each other along a direction parallel to the x axis, and determined the potential of mean force (PMF) as a function of the minimum surface-to-surface interparticle distance d. These results are presented in Fig. 2, together with similar results for spherocylindrical nanoparticles (Sec. III B). The PMF in this case represents the difference in free energy between any given two-particle configuration and a situation where the particles are infinitely apart. Afterwards, we determined the defect structures formed by the nematic around the spherical nanoparticles, when they are separated by a distance $d_{\mathrm{min,nm}}$ corresponding to the minimum in the PMF. 3D visualizations of these defect structures are depicted in Fig. 3(a). In a similar way, we also present in Fig. 3(b) the defect structures observed when two spherical micron-sized particles ($D=1$ μm, ten times larger than the nm-sized particles) are separated by a distance $d=10d_{\mathrm{min,nm}}$.

Our results for two spherical nanoparticles ($W=0.1$ J/m^2) indicate that when the distance d is reduced to about 55 nm, the PMF first becomes slightly positive, suggesting that the particles first experience a repulsion as they approach each other. Visual inspection of the defect structures formed by the nematic at $d=55$ nm (not shown) indicates that the Saturn rings around each particle start to interact with each other, and thus become distorted with respect to the Saturn rings observed when the particles are at $d>55$ nm. These distortions in the Saturn rings cause the total

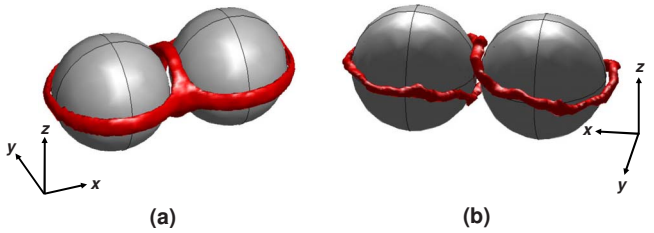

(a) (b)

FIG. 3. (Color online) 3D visualizations of the defect structures formed by the nematic around two spherical particles that are close to each other. (a) nm-sized particles ($D=100$ nm) separated by a distance $d=7.5$ nm (the minimum in the PMF, Fig. 2); the nematic forms an entangled hyperbolic defect structure. (b) μm-sized particles ($D=1$ μm) separated by a distance $d=0.075$ μm; the nematic forms a figure-of-eight defect structure. The defect structure presented in (b) looks more irregular than that in (a), since the minimum length of the finite elements for the case of μm-sized particles is ten times larger than that in the case of nm-sized particles (however, the meshes used in both calculations have a similar number of finite elements)

PMF to become positive [Fig. 2(a)]. These findings are in agreement with results from previous computational studies [12,36]. Previous numerical results [12] also suggest that this initial repulsion decreases in magnitude as the particle size is reduced. Moreover, experimental and numerical results [7] indicate that this repulsion is observed only when both particles approach each other along a plane containing both Saturn rings entirely. This repulsion can be avoided by making one of the spheres to approach the other via an off-center trajectory (i.e., making one of the particles to leave the plane $z=0$ and then come back to this plane at interparticle distances small enough; see, e.g., Fig. 1 in Ref. [7]). Further reductions in d makes the total PMF to become negative, reaching a minimum of about 1500 k_BT at $d_{\mathrm{min,nm}}=7.5$ nm. At this distance, the nematic forms a defect structure consisting of one large Saturn ring (which arises from the fusion of the two Saturn rings that surround each particle when they are far from each other) and a new disclination ring arises. This new ring forms in the interparticle space and is orthogonal to the original Saturn rings around each particle [Fig. 3(a)]. This defect structure was first reported in the computational study of Guzmán *et al.* [12], and was later observed in other computational studies [9,48]. Such a defect structure was also observed experimentally for micron-sized particles by Ravnik *et al.* [9], who termed it the "entangled hyperbolic" defect structure. The results described previously were obtained for two spherical nanoparticles with a surface anchoring strength of $W=0.1$ J/m^2 [Fig. 2(a)]. For the case of two nanospheres with $W=0.01$ J/m^2, the PMF curve [Fig. 2(b)] exhibit the same features previously described for the case of $W=0.1$ J/m^2. The magnitudes of the initial repulsion and the PMF minimum observed for the case of $W=0.01$ J/m^2 [Fig. 2(b)] are very similar to those observed for the case of $W=0.1$ J/m^2 [Fig. 2(a)]. The whole PMF curve for $W=0.01$ J/m^2 is shifted to the left (i.e., towards smaller values of d) when compared to the PMF curve for $W=0.1$ J/m^2 [Fig. 2(a)]. In consequence, the initial repulsion and the PMF minimum for the case of $W=0.01$ J/m^2 [Fig. 2(b)] are observed at slightly smaller interparticle distances

(40 and 5 nm, respectively) when compared to the case of $W=0.1$ J/m^2 [55 and 7.5 nm, respectively; see Fig. 2(a)]. The defect structure observed at $d_{\mathrm{min,nm}}=5$ nm for the case of $W=0.01$ J/m^2, is very similar to that depicted in Fig. 3(a) ($W=0.1$ J/m^2, $d_{\mathrm{min,nm}}=7.5$ nm), and therefore it is not shown here.

In Fig. 3(b) we present the defect structure observed when two spherical μm-sized particles ($D=1$ μm) with $W=0.01$ J/m^2 are at a distance $d=0.075$ μm, equal to ten times the distance at which the minimum in the PMF is observed for nm-sized particles (Fig. 2). Such a choice of interparticle distance was arbitrary and may not correspond to the distance at which the minimum in the PMF is observed for the case of two spherical particles with $D=1$ μm. Nevertheless, the defect structure observed for μm-sized particles separated by an interparticle distance $d=0.075$ μm consists of a single disclination line that surrounds both particles and twists in the interparticle region, forming a figure of eight (as termed by Ravnik *et al.* in Ref. [9]). Such a defect structure was also observed in the computational studies of Araki and Tanaka [48], and in the experimental and computational study of Ravnik *et al.* [9]. We have not included results for the PMF for micron-sized particles; Ravnik *et al.* [9] have already presented results for the energetic interactions between pairs of μm-sized spherical particles. Those results [9] exhibit the same shape and features as those observed by us in this work for nm-sized particles, differing in the values of the interparticle distances d and the magnitude of the energies ($\sim 14\,000$ k_BT at $d/D\sim 1.04$, for two spheres with $D=4.7$ μm [9]).

Our results suggest that pairs of nm-sized spherical particles tend to form entangled hyperbolic defect structures, whereas the nematic around μm-sized particles in close proximity tends to form figure-of-eight defect structures. We note that our calculations typically stated from an initial configuration where the director field $\mathbf{n}(\mathbf{r})$ was aligned parallel to the z direction. For the case of micron-sized particles, we did not attempt to start our simulations from an isotropic phase that is later quenched into the nematic phase; Ravnik *et al.* [9] already did so using both experiments and computer simulations. They report that when the final state consists of entangled defect structures, a figure-of-eight defect is obtained in about 70% of the cases; the rest of the final states consisted of entangled hyperbolic and "figure of omega" structures [9]. They also report that they found entangled structures in 52% of the cases; 48% of the final states were not entangled. For pairs of μm-sized spheres, Ravnik *et al.* [9] and Araki and Tanaka [48] also observed entangled hyperbolic defect structures, but they were metastable. Araki and Tanaka [48] argue that in their calculations, the entangled hyperbolic structures eventually evolve into figure-of-eight structures. In contrast, our results for nm-sized spheres strongly suggest that the entangled hyperbolic defect structure is the most stable. We have repeated our calculations with a pair of nanoparticles with $W=0.1$ and 0.01 J/m^2, separated by their corresponding distance $d_{\mathrm{min,nm}}$ (7.5 and 5 nm, respectively), and starting from 20 different random configurations for $\mathbf{n}(\mathbf{r})$ (i.e., the LC is in an isotropic phase). After quenching the LC into the nematic phase, we always obtained entangled hyperbolic defect structures similar to those observed where we started with the LC directly in the nematic phase. For nm-sized spheres, we did not observe any other entangled or unentangled defect structure, in contrast to what was reported by Ravnik *et al.* [9] and Araki and Tanaka [48] for pairs of μm-sized spheres. Our results also suggest that the most stable defect structure changes from/to a figure of eight to/from an entangled hyperbolic defect, at some point where the particle diameters are between $D=100$ nm and 1 μm. We emphasize that we have not aimed at determining the exact particle size at which the transition occurs. Establishing the transition point would require calculating and comparing the free energies of the entangled defect structures as a function of particle size, including physical situations for which the structures are metastable. Such detailed calculations could be the subject of follow-up studies.

B. Spherocylindrical particles

In this section we present results for the PMF and the defect structures observed when a pair of nm-sized and μm-sized spherocylindrical particles is immersed in a nematic. We have considered spherocylinders with two different aspect ratios $L/D=1.44$ and 3.00, and the particles approach each other in the x-y plane in two ways (Fig. 5): (1) keeping their long axes aligned (linear array) and (2) keeping their long axes parallel (parallel array). Results for the PMF as a function of the minimum surface-to-surface interparticle distance d for nm-sized particles ($D=100$ nm) are presented in Fig. 2(a) for the case of $W=0.1$ J/m^2 and Fig. 2(b) for the case of $W=0.01$ J/m^2. As in the case of spherical particles, the total PMF first becomes positive as the particles approach each other, due to the same reasons previously discussed for spherical nanoparticles. Previous calculations for smaller spherocylindrical nanoparticles [13] did not show any significant repulsion effects, which suggests that a reduction in particle size leads to a decrease in the initial repulsion experienced by the particles as they approach each other. Further reductions in d makes the PMF to become negative, reaching a minimum of ~ 1600 k_BT ($L/D=1.44$, linear), $\sim 1600k_BT$ ($L/D=3.0$, linear), $\sim 2300k_BT$ ($L/D=1.44$, parallel), and $\sim 5400k_BT$ ($L/D=3.0$, parallel). In analogy to what was observed for the case of spherical nanoparticles, the magnitudes of the PMF minima observed for our spherocylindrical nanoparticles seem to be independent of the values of W. The PMF curves observed for spherocylinders are similar for both values of W. For the case of $W=0.01$ J/m^2 [Fig. 2(b)], the interparticle distances at which the maxima and the minima in the PMF curves are observed are slightly smaller, and the whole PMF curves are slightly displaced to smaller distances, when compared to the PMF curves obtained for spherocylinders with $W=0.1$ J/m^2 [Fig. 2(a)].

In Fig. 4(a) we present results for the torque transmitted by the nematic liquid crystal to the spherocylindrical nanoparticles ($D=100$ nm) as they approach each other in the x-y plane. The components of the torque were computed by numerical integration of Eqs. (8) and (9) over the surfaces of each spherocylinder. The magnitude of the components of the torque acting over the first spherocylinder were found to be approximately equal to the magnitude of their counter-

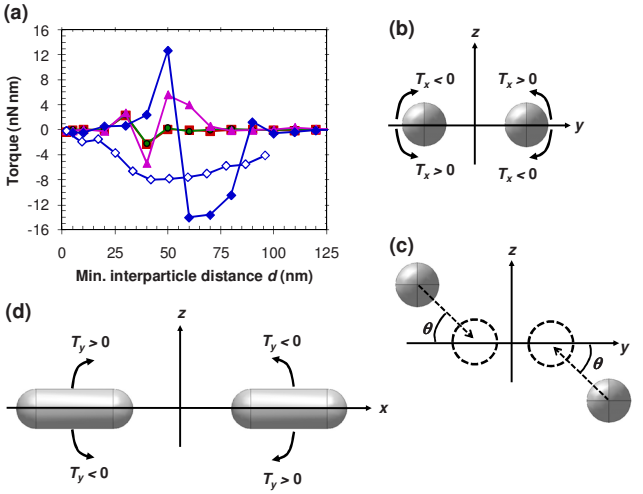

FIG. 4. (Color online) (a) Torque transmitted on each spherocylinder as a function of the minimum surface-to-surface interparticle distance d, for all the systems of two spherocylindrical nanoparticles considered in this study. Closed symbols are for particles approaching each other through the plane $z=0$; open symbols are for particles approaching each other in a diagonal trajectory [Fig. 4(c)]. Diamonds: x component of the torque, spherocylindrical nanoparticles in a parallel array, $L/D=3.00$. Triangles: x component of the torque, spherocylindrical nanoparticles in a parallel array, $L/D=1.44$. Circles: y component of the torque, spherocylindrical nanoparticles in a linear array, $L/D=3.00$. Squares: y component of the torque, spherocylindrical nanoparticles in a linear array, $L/D=1.44$. The rest of the components of the torque that are not depicted here have a value close to zero for all values of d considered here. (b) For a pair of spherocylindrical nanoparticles in a parallel array (their long axes are parallel to the x axis), the torques T_x tend to make the spherocylinders to rotate around their long axis without swinging out of the plane $z=0$; the particles keep their long axes perpendicular to the director field $\mathbf{n}(\mathbf{r})\|z$. (c) Spherocylindrical nanoparticles approaching each other via a diagonal trajectory, where particle 1 is initially in a plane $z>0$ and particle 2 is in a plane $z<0$; both reach the plane $z=0$ when the interparticle distance is small ($d\sim 2$ nm). For the results presented in Fig. 4(a), the angle $\theta=45°$. (d) For a pair of spherocylindrical nanoparticles in a linear array, the torques T_y tend to make the spherocylinders to align with their long axis parallel to the z axis.

parts acting over the second spherocylinder, and therefore in Fig. 4 we have presented the average value of these torques. Furthermore, the results presented in Fig. 4 do not depend on the value of W (the mathematical expressions for the torque only depend on L_1). Our results for spherocylinders that approach each other keeping their long axes parallel (parallel arrays) indicate that $T_y \approx T_z \approx 0$ for all the interparticle distances considered; variations in the magnitude of T_x are observed at some values of d (Fig. 4), suggesting that spherocylinders approaching each other in a parallel array tend to develop torques in the x direction. The torque $T_x \sim 0$ for spherocylinders with $L/D=3.00$ in a parallel array, when they are separated by a distance $d>100$ nm. However, as d is reduced, the value of T_x slightly increases and then goes to negative values, reaching a minimum of ~ -14 nN nm at $d \sim 60$ nm. Such a negative torque in the x direction will tend to make the spherocylinders to rotate around their long axis in a clockwise direction, without swinging out of the plane $z=0$; their long axes are always perpendicular to the director field $\mathbf{n}(\mathbf{r})\|z$ [Fig. 4(b)]. When the interparticle distance decreases from $d\sim 60$ to 50 nm, the torque T_x changes from a negative value ($T_x \sim -14$ nN nm) to a positive value [$T_x \sim 13$ nN nm, see Fig. 4(a)]. Such a positive torque in the x direction will make the spherocylinders to rotate around their long axis in an anticlockwise direction, without swinging out of the plane $z=0$ [Fig. 4(b)]. Further reductions in d make T_x to decrease and go to zero at $d\sim 20$ nm. Similar effects are observed for a pair of spherocylinders with $L/D=1.44$ in a parallel array [Fig. 4(a)]. In this case, the spherocylinders first experience a positive torque ($d\sim 50$ nm), which then becomes negative ($d\sim 40$ nm) before finally decaying to zero ($d\sim 20$ nm). The magnitude of the torques T_x observed for the pair of spherocylinders with $L/D=1.44$ are smaller than those experienced by the larger spherocylinders. The magnitude of the torques T_x acting over the long spherocylinders can be somewhat reduced by making the particles approach each other via a "diagonal" trajectory [Fig. 4(c)]. In this approach, particle 1 is initially in a plane $z<0$ and particle 2 is in a plane $z>0$, and they reach the plane $z=0$ when the interparticle distance is small ($d\sim 2$ nm). When the angle $\theta=45°$ [Fig. 4(c)], our results indicate that the particles still experience a negative nematic torque T_x, but its magnitude decreases by about 45% with respect to the situation where the particles approach each other in the plane $z=0$ [Fig. 4(a)]. Another way to overcome these torques would be to "manually" apply similar torques of the same magnitude and direction but opposite sign.

For pairs of spherocylinders that approach each other keeping their long axes aligned (linear arrays), our results indicate that $T_x \approx T_z \approx 0$ for all the interparticle distances considered, whereas $T_y \neq 0$ for some values of d (Fig. 4). These results suggest that spherocylinders approaching each other in a linear array tend to develop torques in the y direction. These torques T_y tend to rotate the particles and make their long axis to align parallel to the director field $\mathbf{n}(\mathbf{r})\|z$ [Fig. 4(d)]. Previous simulation results for a system containing only one spherocylindrical particle with homeotropic anchoring in a nematic [13,62] indicate that a configuration where the spherocylinder is aligned with its long axis parallel to the director $\mathbf{n}(\mathbf{r})$ has to pay a large free energy penalty [13]; moreover, a nematic torque will develop [62] that will make the particle to align with its long axis perpendicular to the director $\mathbf{n}(\mathbf{r})$. Our results [Fig. 4(a)] also indicate that the magnitude of the torque T_y seems to be independent of the value of L/D. Moreover, these torques T_y are small when compared to the torques T_x experienced by spherocylinders in a parallel array. As a result, rather than a full rotation that will make the particles to align with their long axis parallel to the z direction, particles should only experience small "vibration" effects as they approach each other in a linear array. The alternative discussed previously to overcome the torques in parallel arrays of spherocylinders also applies for particles in a linear array.

The defect structures formed by the nematic when the nanoparticles are separated by an interparticle distance $d_{\mathrm{min,nm}}$ [corresponding to the minimum in the PMF, Fig. 2(a)] are depicted in Fig. 5 for the case of $W=0.1$ J/m^2. The de-

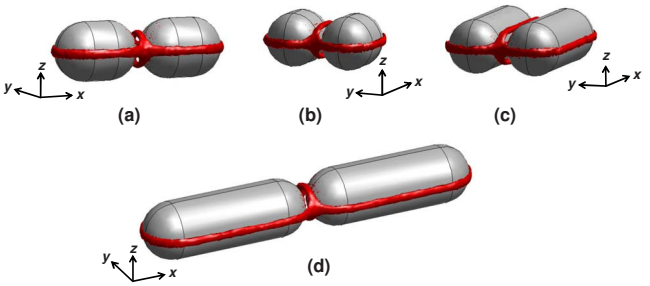

FIG. 5. (Color online) 3D visualizations of the "entangled hyperbolic" defect structures formed by the nematic around two nm-sized spherocylindrical particles that are close to each other (at the distance d at which the PMF reaches its minimum, Fig. 2). (a) $L/D=1.44$, linear array. (b) $L/D=1.44$, parallel array. (c) $L/D=3.00$, parallel array. (d) $L/D=3.00$, linear array.

fect structures observed for nm-sized spherocylinders at a distance $d_{\mathrm{min,nm}}$ for the case of $W=0.01$ J/m^2 are very similar to those depicted in Fig. 5. As found in our previous study [13], and in analogy to what was found for spherical particles, the nematic forms entangled hyperbolic defect structures when the nanoparticles are close to each other. These defect structures consist of one large Saturn ring (which is elongated due to the shape of the nanoparticles, and arises from the fusion of the two Saturn rings that surrounded each particle when they were far from each other), and another disclination ring which is orthogonal to the first large one and forms in the interparticle space. The interparticle disclination ring can be elongated or not depending on the array formed by the particles (parallel or linear, Fig. 5). As we discussed in our previous work [13], the magnitude of the minimum in the PMF depends mainly on the size of the interparticle disclination ring, which is filled with a highly ordered nematic phase. As a result, (1) a parallel array of spherocylindrical nanoparticles exhibits a lower minimum in the PMF, as compared to a linear array of nanoparticles with the same aspect ratio, (2) when the spherocylinders are in a parallel array, nanoparticles with larger values of L/D exhibit lower minima in the PMF, and (3) when the spherocylinders are in a linear array, the minimum in the PMF does not change significantly with L/D. Furthermore, the value of the minimum in the PMF in a linear array of nm-sized spherocylinders is similar to that observed for the case of two spherical nanoparticles with the same diameter (Fig. 2).

For the case of micron-sized spherocylindrical particles with $W=0.01$ J/m^2, in Fig. 6 we present 3D visualizations of the defect structures formed by the nematic when the particles are close to each other, at distances equal to ten times the distance at which the minimum in the PMF is observed for nm-sized particles. As was mentioned when discussing our results for micron-sized spheres, such a choice of interparticle distance is arbitrary and may not correspond to the distance at which the minimum in the PMF is observed for the case of micron-sized spherocylindrical particles. We did not include results for the PMF for micron-sized spherocylinders; these are expected to be similar to those presented in Fig. 2 for nm-sized spherocylinders, differing in the magnitude of the energies and the distances d, as we have discussed for the case of spherical particles (Sec. III A). For the

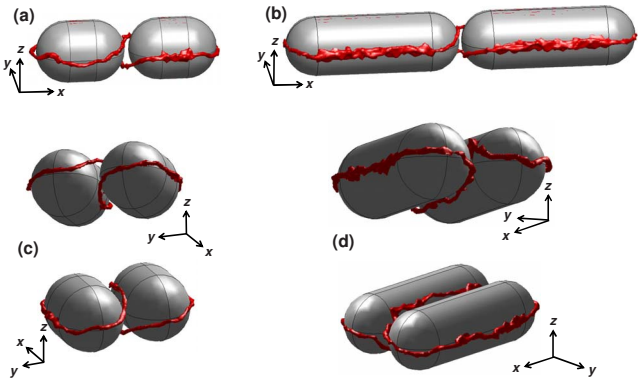

FIG. 6. (Color online) 3D visualizations of the figure-of-eight defect structures formed by the nematic around two μm-sized spherocylindrical particles that are close to each other (at a distance d equal to ten times the distance at which the nm-sized particles reach the minimum in the PMF, Fig. 2). (a) $L/D=1.44$, linear array. (b) $L/D=3.00$, linear array. (c) $L/D=1.44$, parallel array. (d) $L/D=3.00$, parallel array. For (c) and (d), two different views of the same configuration are presented for clarity. The defect structures presented here look more irregular than those presented in Fig. 5, because the minimum length of the finite elements for the case of μm-sized particles is ten times larger than that in the case of nm-sized particles (however, the meshes used in both calculations have a similar number of finite elements)

case of pairs of micron-sized spherocylinders that are close to each other, the nematic forms entangled "figure-of-eight" defect structures around the particles, in analogy to what was observed for micron-sized spherical particles [Fig. 3(b)]. These defect structures are elongated when compared to those observed for spherical particles; the shape of the entangled defect structures naturally depends on the way the spherocylinders approach each other (linear, parallel). We did not attempt to calculate the torques between pairs of micron-sized spherocylindrical particles; these are expected to follow the same trends as those shown in Fig. 4 for nm-sized spherocylinders, with differences in the magnitude of the torques and the distances at which they are observed.

Our results for spherocylindrical particles suggest that pairs of nm-sized particles close to each other tend to form elongated entangled hyperbolic defect structures, whereas the nematic around micron-sized particles tends to form elongated figure-of-eight defect structures. These results are analogous to those obtained for spherical particles (Sec. III A). For each array of nm-sized particles separated by a distance $d_{\mathrm{min,nm}}$ (corresponding to the minimum in the PMF), we repeated our calculations starting from 20 different random configurations for $\mathbf{n}(\mathbf{r})$, as we did for the spherical nanoparticles (Sec. III A), and again we always obtained entangled hyperbolic defect structures; we did not observe any other entangled or unentangled structure. Our results for spherocylindrical particles with L/D between 1.44 and 3.00 also suggest that the most stable defect structure changes from/to a figure of eight to/from an entangled hyperbolic defect, at some point when the particle diameters are between $D=100$ nm and 1 μm. We note again that determining the exact particle size at which the transition between defect structures takes place was not an objective of this study.

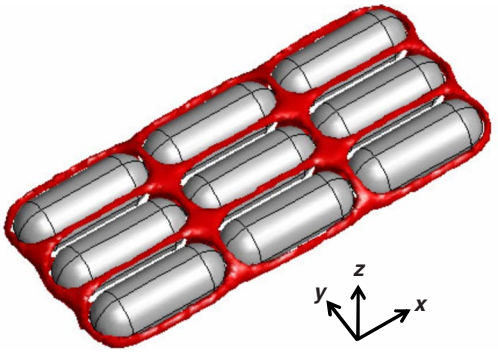

FIG. 7. (Color online) Representation of an ordered structure that could be assembled using spherocylindrical particles immersed in a nematic liquid crystal. The particles are held together by the defects formed by the nematic around the spherocylinders.

Our results suggest that the LC-mediated interactions between pairs of particles are strong and anisotropic, and vary with the shape and dimensions of the particles. These interactions can be used to bind the particles together and assemble them into ordered structures with unconventional morphologies. As an example, in Fig. 7 we depict an ordered structure that could be assembled using spherocylindrical particles immersed in a nematic liquid crystal "sandwiched" between two parallel walls forming a thin cell. The particles would be held together in such an ordered structure by the defects formed by the nematic around the spherocylinders. Such an ordered structure could be assembled in principle following the same ideas of the work presented by Muševič *et al.* [6–10] for the assembly of spherical particles in a nematic. In fact, an experimental study considering systems of rodlike particles in a nematic has been carried out very recently [63], suggesting the feasibility of assembling ordered arrays of these particles in a nematic. Ordered particle structures with symmetries different from the hexagonally close-packed crystals typically formed by spherical colloids could be relevant for applications in photonics and nanoscale optoelectronics [51,52].

IV. CONCLUDING REMARKS

Using a mesoscale theory for the tensor order parameter **Q**, we have investigated the effects of particle size and shape on the quadrupolar (i.e., Saturn-ring-like) defect structures formed by a nematic liquid crystal around pairs of particles that are close to each other. We considered systems of nm-sized and μm-sized particles with spherical and spherocylindrical shapes. Our results for pairs of spherical particles that are in close proximity suggest that the nematic forms entangled hyperbolic defect structures around nm-sized particles, and figure-of-eight defects around micron-sized spheres. The former defect structure consists of one large Saturn ring (which arises from the fusion of the two Saturn rings that surround each particle when they are far from each other) and another disclination ring, which is orthogonal to the first one and forms in the interparticle space [Fig. 3(a)]. The "figure of eight" defect structure consists of a single disclination loop that is twisted in the interparticle space and surrounds both particles [Fig. 3(b)]. According to our calculations, the potential of mean force between two nanospheres ($D=100$ nm) reaches a minimum of $\sim 1500 k_B T$ when the particles are separated by a distance of about 5–7.5 nm. For spherocylindrical particles, we considered two different aspect ratios ($L/D=1.44$ and 3.00), and two different arrangements for the particles (linear and parallel). Results for all these systems follow the same trends observed for spherical particles: the nematic forms entangled hyperbolic defects around the nm-sized particles ($D=100$ nm, Fig. 5), and figure-of-eight defects around the μm-sized spherocylinders ($D=1$ μm, Fig. 6). These entangled defect structures exhibit distorted shapes as compared to those observed for spheres, due to the spherocylindrical shape of the particles and their arrangement in linear or parallel arrays. For spherocylindrical nanoparticles, the potential of mean force depends directly on the size of the third disclination ring that forms in the interparticle region. As a result, the potential of mean force (PMF) can reach a minimum of $\sim 5700 k_B T$ for the case of spherocylindrical nanoparticles with $L/D=3.0$, when their long axis are parallel and they are close to each other. For all our systems of nm-sized particles, we have considered two values for the surface anchoring strength, $W=0.01$ and 0.1 J/m^2. The curves of PMF vs interparticle distance d for $W=0.01$ J/m^2 are shifted to the left (i.e., towards smaller values of d) when compared to the PMF curves observed for $W=0.1$ J/m^2 (Fig. 2). The values of the maxima and minima in the PMF curves seem to be unaffected by the choice of W for the systems considered in this study (Fig. 2). Although we have not determined the exact particle diameter at which the transition between entangled defect structures takes place, our results for spherical and spherocylindrical particles ($L/D=1.44$ and 3.00) suggest that such a transition occurs when the particle diameters are between $D=100$ nm and 1 μm. Our results for pairs of nm-sized spherical and spherocylindrical particles that are in close proximity strongly suggest that the entangled hyperbolic defect structure is the most stable configuration, as we did not observe any other entangled or unentangled defect structure. Such an observation contrasts to the results of Ravnik *et al.* [9] for pairs of μm-sized spheres, which form entangled structures in 52% of the cases; of these, in 70% of the cases a figure-of-eight defect structure is formed, and in 30% the nematic forms metastable entangled hyperbolic and figure-of-omega structures around the particles.

We have also calculated the torques that develop when pairs of spherocylindrical nanoparticles immersed in a nematic approach each other. Spherocylinders approaching each other in the plane $z=0$ with their long axis parallel to each other develop torques in the x direction at intermediate values of interparticle distances d (Fig. 4). The magnitude of these torques depend on the L/D ratio of the particles, and tends to make the particles to rotate around their long axis without swinging out of the plane $z=0$ where their long axes are initially located. These torques T_x change signs in a small range of values of d (e.g., $d=50$–60 nm for the case of $L/D=3.00$), and become equal to zero at large and small values of d. Particles in a linear array, in contrast, develop torques in the y direction as they approach each other. These torques T_y tend to rotate the particles to align them with their

long axis parallel to $\mathbf{n}(\mathbf{r}) \| z$. The magnitude of these torques T_y is very small when compared to the nematic torques T_x observed for spherocylinders in a parallel array. These torques can be somewhat reduced by making the particles approach each other via a "diagonal" trajectory [Fig. 4(c)]; our results indicate that the particles still experience a negative nematic torque T_x as they approach, but its magnitude decreases by about 45% with respect to the situation where the particles approach each other in the plane $z=0$ [Fig. 4(a)].

Our results suggest that the LC-mediated interactions between pairs of particles are strong and anisotropic, and vary with the shape and dimensions of the particles. These interactions can be used to bind the particles together and assemble them into ordered structures with unconventional morphologies. Similar studies for particles with shapes other than spherical, spherocylindrical and cubic immersed in LCs are currently underway in our group, and could be relevant for ongoing research in light-scattering devices, electro-optical switches, photonics, nanoscale electronics, displays, and optical sensors.

ACKNOWLEDGMENTS

F.R.H. thanks Shivkumar Bale (LSU) for his assistance with the torque calculations, and is grateful to Erik Santiso (MIT) for very helpful and enlightening discussions.

[1] P. Poulin, H. Stark, T. C. Lubensky, and D. A. Weitz, Science **275**, 1770 (1997); P. Poulin, V. Cabuil, and D. A. Weitz, Phys. Rev. Lett. **79**, 4862 (1997); P. Poulin and D. A. Weitz, Phys. Rev. E **57**, 626 (1998); J. C. Loudet, P. Barois, and P. Poulin, Nature (London) **407**, 611 (2000).

[2] V. G. Nazarenko, A. B. Nych, and B. I. Lev, Phys. Rev. Lett. **87**, 075504 (2001); I. I. Smalyukh, S. Chernyshuk, B. I. Lev, A. B. Nych, U. Ognysta, V. G. Nazarenko, and O. D. Lavrentovich, *ibid.* **93**, 117801 (2004).

[3] M. Yada, J. Yamamoto, and H. Yokoyama, Langmuir **18**, 7436 (2002); Phys. Rev. Lett. **92**, 185501 (2004).

[4] A. B. Nych, U. M. Ognysta, V. M. Pergamenshchik, B. I. Lev, V. G. Nazarenko, I. Muševič, M. Škarabot, and O. D. Lavrentovich, Phys. Rev. Lett. **98**, 057801 (2007); U. Ognysta, A. Nych, V. Nazarenko, I. Muševič, M. Škarabot, M. Ravnik, S. Žumer, I. Poberaj, and D. Babič, *ibid.* **100**, 217803 (2008).

[5] K. Kita, M. Ichikawa, and Y. Kimura, Phys. Rev. E **77**, 041702 (2008).

[6] I. Muševič, M. Škarabot, U. Tkalec, M. Ravnik, and S. Žumer, Science **313**, 954 (2006).

[7] M. Škarabot, M. Ravnik, S. Žumer, U. Tkalec, I. Poberaj, D. Babič, and I. Muševič, Phys. Rev. E **77**, 061706 (2008).

[8] M. Škarabot, M. Ravnik, S. Žumer, U. Tkalec, I. Poberaj, D. Babič, N. Osterman, and I. Muševič, Phys. Rev. E **76**, 051406 (2007).

[9] M. Ravnik, M. Škarabot, S. Žumer, U. Tkalec, I. Poberaj, D. Babič, N. Osterman, and I. Muševič, Phys. Rev. Lett. **99**, 247801 (2007).

[10] M. Škarabot, M. Ravnik, S. Žumer, U. Tkalec, I. Poberaj, D. Babič, N. Osterman, and I. Muševič, Phys. Rev. E **77**, 031705 (2008).

[11] K. Takahashi, M. Ichikawa, and Y. Kimura, Phys. Rev. E **77**, 020703 (2008).

[12] O. Guzmán, E. B. Kim, S. Grollau, N. L. Abbott, and J. J. de Pablo, Phys. Rev. Lett. **91**, 235507 (2003); S. Grollau, E. B. Kim, O. Guzmán, N. L. Abbott, and J. J. de Pablo, J. Chem. Phys. **119**, 2444 (2003); E. B. Kim, O. Guzmán, S. Grollau, N. L. Abbott, and J. J. de Pablo, *ibid.* **121**, 1949 (2004); O. Guzmán, N. L. Abbott, and J. J. de Pablo, J. Polym. Sci., Part B: Polym. Phys. **43**, 1033 (2005).

[13] F. R. Hung, O. Guzmán, B. T. Gettelfinger, N. L. Abbott, and J. J. de Pablo, Phys. Rev. E **74**, 011711 (2006).

[14] F. R. Hung, B. T. Gettelfinger, G. M. Koenig Jr., N. L. Abbott, and J. J. de Pablo, J. Chem. Phys. **127**, 124702 (2007).

[15] T. Hegmann, H. Qi, and V. M. Marx, J. Inorg. Organomet. Polym. Mater. **17**, 483 (2007); H. Qi and T. Hegmann, J. Mater. Chem. **18**, 3288 (2008); J. P. F. Lagerwall and G. Scalia, J. Mater. Chem. **18**, 2890 (2008); C. Zakri, Liq. Cryst. Today **16**, 1 (2007).

[16] H. Qi and T. Hegmann, J. Mater. Chem. **16**, 4197 (2006); H. Qi, A. Lepp, P. A. Heiney, and T. Hegmann, *ibid.* **17**, 2139 (2007).

[17] M. Mitov, C. Bourgerette, and F. de Guerville, J. Phys.: Condens. Matter **16**, S1981 (2004).

[18] M. C. W. van Boxtel, R. H. C. Janssen, D. J. Broer, H. T. A. Wilderbeek, and C. W. M. Bastiaansen, Adv. Mater. (Weinheim, Ger.) **12**, 753 (2000).

[19] S. R. Nersisyan and N. V. Tabiryan, Appl. Phys. Lett. **88**, 151106 (2006).

[20] P. A. Kossyrev, A. Yin, S. G. Cloutier, D. A. Cardimona, D. Huang, P. M. Alsing, and J. M. Xu, Nano Lett. **5**, 1978 (2005).

[21] C. Lapointe, A. Hultgren, D. M. Silevitch, E. J. Felton, D. H. Reich, and R. L. Leheny, Science **303**, 652 (2004).

[22] M. D. Lynch and D. L. Patrick, Nano Lett. **2**, 1197 (2002); Chem. Mater. **16**, 762 (2004).

[23] I. Dierking, G. Scalia, P. Morales, and D. LeClere, Adv. Mater. (Weinheim, Ger.) **16**, 865 (2004).

[24] P. van der Schoot, V. Popa-Nita, and S. Kralj, J. Phys. Chem. B **112**, 4512 (2008).

[25] V. K. Gupta, J. J. Skaife, T. B. Dubrovsky, and N. L. Abbott, Science **279**, 2077 (1998); R. R. Shah and N. L. Abbott, *ibid.* **293**, 1296 (2001); J. M. Brake, M. K. Daschner, Y. Y. Luk, and N. L. Abbott, *ibid.* **302**, 2094 (2003); G. M. Koenig Jr., M.-V. Meli, J.-S. Park, J. J. de Pablo, and N. L. Abbott, Chem. Mater. **19**, 1053 (2007); G. M. Koenig Jr., B. T. Gettelfinger, J. J. de Pablo, and N. L. Abbott, Nano Lett. **8**, 2362 (2008).

[26] E. Tjipto, K. D. Cadwell, J. F. Quinn, A. P. R. Johnston, N. L. Abbott, and F. Caruso, Nano Lett. **6**, 2243 (2006).

[27] S. V. Shiyanovskii, T. Schneider, I. I. Smalyukh, T. Ishikawa, G. D. Niehaus, K. J. Doane, C. J. Woolverton, and O. D. Lavrentovich, Phys. Rev. E **71**, 020702(R) (2005).

[28] J. Müller, C. Sönnichsen, H. von Poschinger, G. von Plessen,

T. A. Klar, and J. Feldmann, Appl. Phys. Lett. **81**, 171 (2002).
[29] S. Grollau, O. Guzmán, N. L. Abbott, and J. J. de Pablo, J. Chem. Phys. **122**, 024703 (2005); O. Guzmán, N. L. Abbott, and J. J. de Pablo, *ibid.* **122**, 184711 (2005).
[30] D. K. Hwang and A. D. Rey, J. Chem. Phys. **125**, 174902 (2006).
[31] R. Mohanraj and H. L. Wu, Sens. Lett. **5**, 538 (2007).
[32] P. G. de Gennes and J. Prost, *The Physics of Liquid Crystals* 2nd ed. (Clarendon, Oxford, 1993).
[33] H. Stark, Phys. Rep. **351**, 387 (2001).
[34] O. Mondain-Monval, J. C. Dedieu, T. Gulik-Krzywicki, and P. Poulin, Eur. Phys. J. B **12**, 167 (1999).
[35] Y. Gu and N. L. Abbott, Phys. Rev. Lett. **85**, 4719 (2000).
[36] R. W. Ruhwandl and E. M. Terentjev, Phys. Rev. E **55**, 2958 (1997); **56**, 5561 (1997).
[37] T. C. Lubensky, D. Pettey, N. Currier, and H. Stark, Phys. Rev. E **57**, 610 (1998).
[38] H. Stark, Eur. Phys. J. B **10**, 311 (1999).
[39] J. Fukuda, M. Yoneya, and H. Yokoyama, Eur. Phys. J. E **13**, 87 (2004).
[40] G. de Luca and A. D. Rey, J. Chem. Phys. **126**, 094907 (2007); **127**, 104902 (2007).
[41] G. Skačej and C. Zannoni, Phys. Rev. Lett. **100**, 197802 (2008).
[42] C. Völtz, Y. Maeda, Y. Tabe, and H. Yokoyama, Phys. Rev. Lett. **97**, 227801 (2006).
[43] J. C. Loudet and P. Poulin, Phys. Rev. Lett. **87**, 165503 (2001).
[44] S. Grollau, N. L. Abbott, and J. J. de Pablo, Phys. Rev. E **67**, 011702 (2003).
[45] J. Fukuda, H. Stark, M. Yoneya, and H. Yokoyama, Phys. Rev. E **69**, 041706 (2004); J. Fukuda and H. Yokoyama, Phys. Rev. Lett. **94**, 148301 (2005).
[46] D. L. Cheung and M. P. Allen, Phys. Rev. E **74**, 021701 (2006); D. L. Cheung and M. P. Allen, Langmuir **24**, 1411 (2008).
[47] R. Yamamoto, Phys. Rev. Lett. **87**, 075502 (2001); R. Yamamoto, Y. Nakayama, and K. Kim, J. Phys.: Condens. Matter **16**, S1945 (2004).
[48] T. Araki and H. Tanaka, Phys. Rev. Lett. **97**, 127801 (2006).
[49] N. Sulaiman, D. Marenduzzo, and J. M. Yeomans, Phys. Rev. E **74**, 041708 (2006).
[50] C. Zhou, P. Yue, and J. J. Feng, Langmuir **24**, 3099 (2008).
[51] S. C. Glotzer, Science **306**, 419 (2004); S. C. Glotzer and M. J. Solomon, Nature Mater. **6**, 557 (2007).
[52] O. D. Velev, Science **312**, 376 (2006).
[53] V. K. Gupta and N. L. Abbott, Science **276**, 1533 (1997).
[54] A. N. Beris and B. J. Edwards, *Thermodynamics of Flowing Systems with Internal Microstructure* (Oxford University Press, New York, 1994).
[55] B. J. Edwards and A. N. Beris, J. Rheol. **33**, 1189 (1989); B. J. Edwards, A. N. Beris, and M. Grmela, J. Non-Newtonian Fluid Mech. **35**, 51 (1990).
[56] N. Schopohl and T. J. Sluckin, Phys. Rev. Lett. **59**, 2582 (1987).
[57] COMSOL Multiphysics™ Version 3.4 User's Guide, COMSOL, Inc., Burlington, MA (2007), and references therein. http://www.comsol.com/
[58] For the case of Eq. (7), the elastic term $L_1\partial_k\partial_k Q_{ij}$ and the Landau–de Gennes terms were included as part of the diffusive flux (c) and source (f) terms, respectively, of the coefficient PDE form of COMSOL Multiphysics™. The constraints given by Eq. (8) where included as part of Neumann boundary conditions. The models were created, executed and saved as MATLAB®.m files.
[59] S. Kralj, E. G. Virga, and S. Žumer, Phys. Rev. E **60**, 1858 (1999); S. Kralj and E. G. Virga, J. Phys. A **34**, 829 (2001); Phys. Rev. E **66**, 021703 (2002).
[60] A. C. Callan-Jones, R. A. Pelcovits, V. A. Slavin, S. Zhang, D. H. Laidlaw, and G. B. Loriot, Phys. Rev. E **74**, 061701 (2006).
[61] G. McKay and E. G. Virga, Phys. Rev. E **71**, 041702 (2005).
[62] D. Andrienko, M. P. Allen, G. Skačej, and S. Žumer, Phys. Rev. E **65**, 041702 (2002).
[63] U. Tkalec, M. Škarabot, and I. Muševic, Soft Matter **4**, 2402 (2008).